energies

MDPI

Article

Composition and Injection Angle Effects on Combustion of an $NH_3/H_2/N_2$ Jet in an Air Crossflow

Donato Cecere [1], Matteo Cimini [1], Simone Carpenella [2], Jan Caldarelli [2] and Eugenio Giacomazzi [1,*]

[1] Laboratory of Sustainable Combustion and Advanced Thermal and Thermodynamic Cycles, Agenzia Nazionale per le Nuove Tecnologie, l'Energia e lo Sviluppo Economico Sostenibile (ENEA), 00124 Rome, Italy; donato.cecere@enea.it (D.C.); matteo.cimini@enea.it (M.C.)
[2] Department of Civil, Computer Science and Aeronautical Technologies Engineering, Roma Tre University, 00146 Rome, Italy; simone.carpenella@uniroma3.it (S.C.); jan.caldarelli@stud.uniroma3.it (J.C.)
* Correspondence: eugenio.giacomazzi@enea.it

Abstract: This study explores the combined effects of fuel composition and injection angle on the combustion behavior of an $NH_3/H_2/N_2$ jet in an air crossflow by means of high-fidelity Large Eddy Simulations (LESs). Four distinct fuel mixtures derived from ammonia partial decomposition, with hydrogen concentrations ranging from 15% to 60% by volume, are injected at angles of 90° and 75° relative to the crossflow, and at operating conditions frequently encountered in micro-gas turbines. The influence of strain on peak flame temperature and NO formation in non-premixed, counter-flow laminar flames is first examined. Then, the instantaneous flow features of each configuration are analyzed focusing on key turbulent structures, and time-averaged spatial distributions of temperature and NO in the reacting region are provided. In addition, statistical analysis on the formation pathways of NO and H_2 is performed, revealing unexpected trends: in particular, the lowest hydrogen content flame yields higher temperatures and NO production due to the enhancement of the ammonia-to-hydrogen conversion chemical mechanism, thus promoting flame stability. As the hydrogen concentration increases, this conversion decreases, leading to lower NO emissions and unburned fuel, particularly at the 75° injection angle. Flames with a 90° injection angle exhibit a more pronounced high-temperature recirculation zone, further driving NO production compared with the 75° cases. These findings provide valuable insights into optimizing ammonia–hydrogen fuel blends for high-efficiency, low-emission combustion in gas turbines and other applications, highlighting the need for a careful balance between fuel composition and injection angle.

Keywords: hydrogen; ammonia; LES; jet in crossflow; combustion

check for updates

Citation: Cecere, D.; Cimini, M.; Carpenella, S.; Caldarelli, J.; Giacomazzi, E. Composition and Injection Angle Effects on Combustion of an $NH_3/H_2/N_2$ Jet in an Air Crossflow. *Energies* **2024**, *17*, 5032. https://doi.org/10.3390/en17205032

Academic Editors: Roberta De Robbio and Maria Cristina Cameretti

Received: 13 September 2024
Revised: 4 October 2024
Accepted: 6 October 2024
Published: 10 October 2024

1. Introduction

The interaction of a jet with a crossflow is a fundamental fluid dynamics phenomenon found in several engineering applications, such as gas turbines, internal combustion engines, and industrial furnaces. In axial-fuel-staged (AFS) combustion, the chamber is divided into two axial zones [1,2]: the primary combustion stage, where initial fuel combustion occurs, and the secondary stage, where additional fuel is injected transversely into the high-temperature main flow via a nozzle. The secondary fuel is thermally ignited in this hot, oxygen-depleted environment, enhancing combustion efficiency. The benefit of AFS combustion with a reacting jet in the secondary stage crossflow is its ability to lower NO_x emissions [3–5]. In the primary stage, high temperatures that typically lead to significant NO_x formation are avoided. Meanwhile, the secondary combustion stage achieves the high turbine inlet temperatures required by advanced J-class turbines, but with minimal residence time, preventing excess NO_x production [6]. Optimal NO_x reduction is achieved through ideal mixing of the secondary fuel with the high-temperature main flow before ignition, avoiding hot spots in AFS technology. This can be facilitated by slower ignition, promoting better mixing between the fuel and the hot main flow, with the flame front forming downstream along the jet trajectory. By adjusting parameters such as the primary stage equivalence ratio and the fuel injection method, the flame dynamics and emissions of the partially premixed reacting jet in crossflow can be effectively controlled. So, a reactive jet within a crossflow is a critical aspect for the design of gas turbine burners based on micro-mixing combustion strategies of hydrogen [7–9] and ammonia/hydrogen blends [10].

In recent years, ammonia has been identified as a potential high-efficiency alternative to hydrocarbon fuels for gas turbine engines [11]. Compared with hydrogen, it offers significant advantages as a fuel due to its higher density, and easier storage and handling. However, ammonia combustion presents several challenges, including low flame speed, temperature, and reactivity, as well as a propensity for high NO_x emissions [12,13]. Nevertheless, given the advantages of ammonia in terms of distribution and storage over hydrogen, in many cases it is feasible to consider generating the necessary hydrogen for co-firing processes by locally decomposing a part of the available ammonia supply.

The characteristics of partially decomposed NH_3-air flames has been the subject of several investigations [14], which have aided in the development of thermal decomposition technologies. Moreover, other studies [15,16] have achieved successful power generation by employing catalytic methods with cracked ammonia as a fuel. In recent years, blending ammonia with hydrogen has demonstrated potential for improving combustion performance and stability [13,17], mitigating pure ammonia combustion issues. Hayakawa et al. [18] demonstrated the potential for efficient ammonia combustion by enhancing flame reactivity and stability through hydrogen addition. Other studies indicated that increasing the ammonia content in the fuel blend tends to promote lean blowout but suppresses flashback. This effect is especially pronounced when ammonia concentration exceeds 70%. Given these conditions, an increase in the equivalence ratio keeping constant the flow rate can help prevent flashback, resulting instead in rich blowout, thereby expanding the overall stable operating range [19]. Research conducted by Khateeb [19,20] demonstrated that incorporating nitrogen into an ammonia–hydrogen blend leads to decreased nitrogen oxide emissions, an expanded lean flammability range, and a reduction in flashback propensity. Valera-Medina et al. [21] investigated the combustion of various ammonia–methane blends in a generic swirl burner for gas turbine applications. While they observed reduced CO and NO_x emissions at elevated equivalence ratios (above 1.10), their findings also highlighted the inadequacy of traditional injection methods for ammonia-based fuels.

In recent years, there has been a growing interest in the combustion of a jet in crossflow (JICF) due to its relevance to practical applications. Experimental studies have employed various diagnostic techniques, such as particle image velocimetry (PIV) and planar laser-induced fluorescence (PLIF) [22,23], gas sampling [24], and emission spectroscopy [25], to characterize the flow field, mixing, and combustion processes. These studies have provided valuable qualitative and quantitative data on flame structure, pollutant formation, and combustion efficiency. However, experimental investigations are often limited by the complexity of the flow field and the difficulty in accessing key regions of interest, hindering detailed measurements.

With the advancement of computational resources and turbulence modeling, CFD simulations have gained prominence in JICF research, offering the ability to access detailed information about the flow field and combustion chemistry at a level of detail that is often impractical to achieve experimentally. Numerical studies have provided valuable insights into the flow structure, jet breakup, and vortex dynamics [26–28]. Despite the great effort, accurate prediction of turbulent mixing and scalar transport remains a challenge, requiring careful selection of turbulence models and grid resolution. From the combustion point of view, several studies have investigated the effects of the velocity ratio, momentum flux ratio, and fuel type on combustion characteristics [29–32]. Nevertheless, while some studies have considered the influence of fuel composition or injection angle individually [33–35], a comprehensive investigation of their combined effects is still lacking. Moreover, early studies employed simplified combustion models, such as flamelet models [36,37] or eddy dissipation concept (EDC) models [38,39], to capture the overall combustion behavior. While these models provide qualitative insights, they may not accurately predict detailed flame structure and pollutant formation.

This study aims to investigate combustion of an ammonia/hydrogen blend jet in an air crossflow, focusing on the effects of the jet composition and its injection angle, quantifying their impact on the jet penetration, mixing, ignition, flame stabilization, and pollutant generation. The methodology adopted in the investigation is based on numerical simulations: chemical kinetics analysis in simple reactors will provide fundamental results on NO_x reaction paths in laminar flames, while high-fidelity Large Eddy Simulations (including accurate models to capture the flame structure and pollutant formation) will provide not only insights into the more complex turbulence/combustion interaction, but also new results on the combined effects of fuel composition and injection angle. The manuscript is structured in the following manner: Section 2 analyzes the NO generation in laminar non-premixed flames using fuels with the same composition as the test matrix mixtures across various strain rates; Section 3 details the LES setup; Section 4 presents the obtained results, emphasizing both instantaneous and time-averaged flow and flame features, analyzing the main combustion formation pathways of NO and H_2, and estimating the pollutants' formation; and conclusions are finally given in Section 5.

2. Chemical Kinetics Analysis

Since unsteady strain is imposed on the fuel and oxidant by turbulent vortices in high-velocity diffusion flames, this section examines the influence of varying strain rates on non-premixed, counter-flow laminar flames. The fuel mixtures and pressure (5 bar) in this analysis match the compositions and pressure adopted in the LES numerical computations. A numerical study using OpenSMOKE++ software [40] is performed to determine the maximum temperature of the flame and NO levels across a range of strain rates up to extinction. The thermal diffusion (Soret) effect is embedded into the species transport equations, and mixture-averaged diffusion coefficients for individual species are taken into account [41].

The panel of Figure 1 illustrates the axisymmetric configuration of the counter-flow flame. The global strain rate, χ, is calculated according to Puri and Seshadri [42]:

$$\chi = \frac{2|u_O|}{L}\left[1 + \frac{|u_F|}{|u_O|}\sqrt{\frac{\rho_F}{\rho_O}}\right], \quad (1)$$

where ρ is the density, and u is the speed of oxidizer (F) and fuel (O) divided by length L.

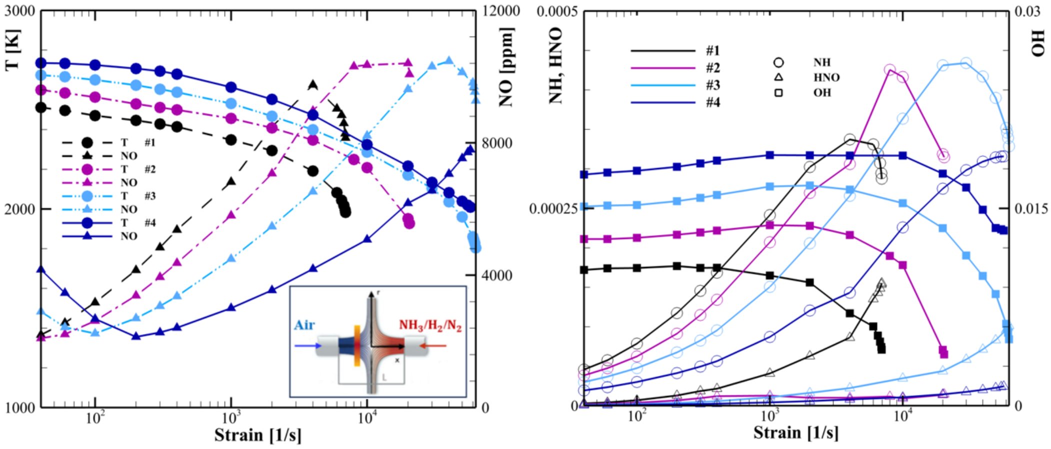

Figure 1. Results of the non-premixed, laminar counter-flow flames at 5 bar with respect to the strain rate [1/s] for the four different mixture; on the left: temperature peak (circle) and NO peak emissions (delta); on the right: NH (circle), HNO (delta), and OH (square) peak mole fractions.

Adaptive mesh refinement is adopted, with relative and absolute error tolerances set to 10^{-6} and 10^{-12}, respectively, for the nonlinear equation iterative process. In NH_3-H_2/air combustion, the front of the flame is located on the stagnation plane (oxidizer side). Quenching conditions are determined by progressively increasing the strain rate from a stable, low-strain flame until extinction occurs. The reaction mechanism employed aligns with that of the LES simulations, and it was selected due to its optimized performance for laminar burning speeds in fuel-rich conditions (up to ϕ =1.8) at pressures between 1 and 5 bar [43].

Figure 1 shows the temperature and NO concentration trends (on the left) as well as the NH, HNO, and OH mass fraction trends (on the right) with respect to the strain rate for the four mixture compositions studied in this work. The increasing hydrogen content in the mixture influences the maximum strain limit that the flame can sustain before it quenches. The flame of the mixture with 15% hydrogen volume (high ammonia content) is extinguished at 7k 1/s, whereas this value increases by increasing the hydrogen content to about 60k 1/s in the mixtures with 45% (3) and 60% (4) of hydrogen. The temperature exhibits a decreasing trend with increasing strain for all the compositions, whereas NO increases almost up to the quenching. Mixture 1 shows a lower temperature and higher NO concentration at the same strain value; however, mixtures 2 and 3 have a higher NO peak of 10% because it survives at larger strains. This behavior can be analyzed through the radicals trend and the pathways study shown in Figures 1 and 2, respectively. Figure 2 reports normalized NO formation rates for different reaction pathways [44], emphasizing the role of each pathway at two strain rates of the mixtures [45]. As the strain and the ammonia composition increase (hydrogen content decreases), the thermal NO formation path becomes less significant due to the lower OH production, while the fuel pathway gains prominence due to the increase in NH and HNO concentrations. Consequently, even with a decreasing thermal path contribution, NO levels reach approximately 10,000 ppm through the dominant fuel pathway before quenching for all mixtures except for the mixture with 60% hydrogen, which reaches 8000 ppm due to the fuel path having a lower impact on the NO formation.

Overall, a higher strain increases the fuel path contribution and reduces the thermal path. However, this behavior is less strong when the hydrogen content increases: for a high hydrogen composition (60% H_2), the opposite trend is observed.

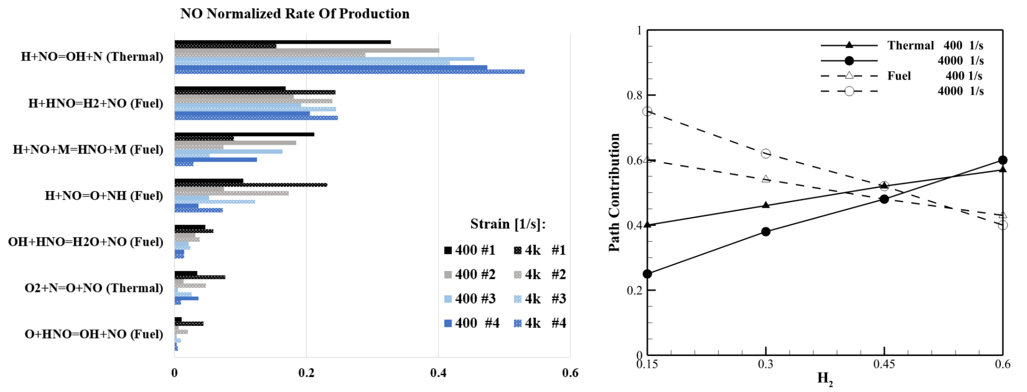

Figure 2. NO formation rate for various reactions associated with thermal and fuel production pathways, along with the relative contribution of the NO production path.

3. Computational Setup

The Navier–Stokes equations governing compressible fluid flow are solved to investigate the combustion characteristics of reactive jets of $NH_3/H_2/N_2$ fuel in an air crossflow of heated non-vitiated air at the pressure of 5 bar, temperature of 850 K, and velocity of 40 m/s.

The simulations are divided into four sets with different fuel mixture compositions. Each set consists of two simulations differing in the fuel injection angle (α) with respect to the crossflow of 90° (case a) and 75° (case b), respectively. The fuel composition varies between the sets, with a hydrogen concentration that ranges from 15% to 60% (by volume), spaced by 15%. These fuel mixture compositions have been chosen since a reduction in NO emission is expected to occur for lower hydrogen percentages [46]. However, the hydrogen content reduction may impact the flame stability [47] and this effect is expected to be even more relevant at a reduced fuel mixture injection angle [35].

In all cases, the fuel is injected with the same pressure of the crossflow, a momentum $\rho_j u_j = 143\,\mathrm{kg/m^2/s}$ and a temperature $T_j = 750\,\mathrm{K}$, which is consistent with the thermal cracking of ammonia. The jet exit hole has a diameter of 2 mm and it is located at the bottom wall. The center of the jet exit coincides with the system's origin. The flow inlet conditions for all simulations are summarized in Table 1.

At the air crossflow inlet of the computational domain, velocity fluctuations are prescribed: approximately 5% of the average inflow speed. Turbulent speed fluctuations are not introduced at the jet exit [35]; this presumption was already justified in our previous work [10], assuming that turbulence of the crossflow is of greater importance than the jet one. At the bottom wall, located at $y = 0$, is applied a boundary condition of a no-slip adiabatic solid surface. On the contrary, the top wall, located at $y = 0.02$ m, is considered adiabatic and Eulerian. The flow is directed out through a non-reflecting outlet, while periodicity is implemented along the spanwise direction. A representation of the boundary conditions is depicted in Figure 3.

Table 1. Conditions at the flow inlets.

	Jet Flow				**Cross Flow**
	Set #1	**Set #2**	**Set #3**	**Set #4**	**-**
Species	$NH_3/H_2/N_2$	$NH_3/H_2/N_2$	$NH_3/H_2/N_2$	$NH_3/H_2/N_2$	O_2/N_2
Composition (% by vol.)	80/15/5	60/30/10	40/45/15	20/60/20	21/79
Pressure (bar)	5	5	5	5	5
Velocity (m/s)	115	131	150	175	40
Temperature (K)	750	750	750	750	850
Density (kg/m^3)	1.2453	1.0924	0.9558	0.8193	2.0411
Viscosity (kg/m/s)	$2.7714 \cdot 10^{-5}$	$2.8130 \cdot 10^{-5}$	$2.8437 \cdot 10^{-5}$	$2.8665 \cdot 10^{-5}$	$3.8510 \cdot 10^{-5}$
Injection angle, $\alpha(°)$	90 (a) and 75 (b)	90 (a) and 75 (b)	90 (a) and 75 (b)	90 (a) and 75 (b)	-
Momentum flux ratio, $J = \rho_j u_j^2 / \rho_{cf} u_{cf}^2$	5.04	5.74	6.58	7.68	-
Velocity ratio, $r = u_j / u_{cf}$	2.87	3.27	3.75	4.37	-
Jet Reynolds number, Re_j	6740	5825	5042	4287	-

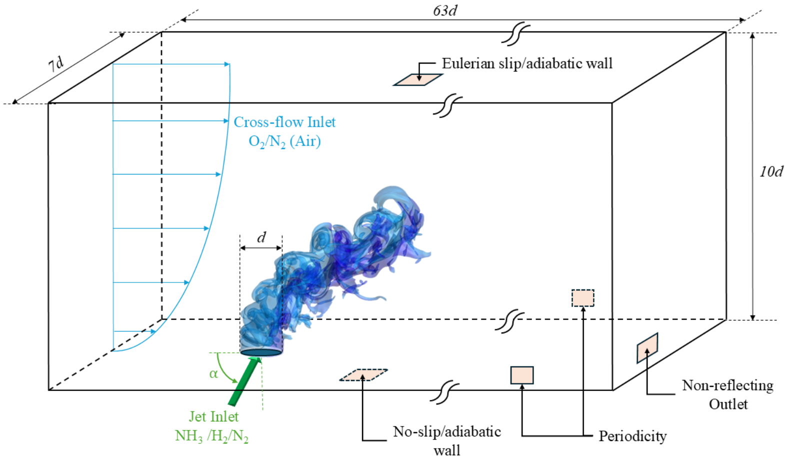

Figure 3. Sketch of the numerical domain and the corresponding boundary conditions for the LES simulations.

The computational domain has an extent of $L_x \times L_y \times L_z = 63\ d \times 10\ d \times 7\ d$, respectively, in the streamwise, wall-normal, and spanwise directions. The grid provides an adequate resolution of the flame structure and larger turbulence scales, from a LES approach point of view: $\Delta x \approx 110$ µm, $\Delta y \approx 35$ µm, and $\Delta z \approx 20$ µm are applied where $x/d \in [-0.5, 3.5]$, $y/d \in [1, 4]$, and $z/d \in [-0.7, 0.7]$. The resolution along the streamwise direction has been chosen to be finer for a detailed analysis of the flow evolution. The maximum grid sizes adopted in less important areas, such as the outlet, are $\Delta x = 220$ µm, $\Delta y = 135$ µm, and $\Delta z = 80$ µm, achieved with an algebraic stretching. Considering the mesh globally, it has 96M cells, with $L_x \times L_y \times L_z = 600 \times 400 \times 400$. The time step used in the simulations is approximately $1.25 \cdot 10^{-9}$ s across all cases, ensuring numerical stability and accurate resolution of the transient flow dynamics. In Table 2, the grid characteristics and the domain dimensions, alongside some other relevant characteristics of the numerical experiment, are summarized.

Table 2. Key attributes of the numerical setup.

Jet exit diameter, d (m)	0.002
Domain extent, $L_x \times L_y \times L_z$	$63\ d \times 10\ d \times 7\ d$
Grid size, $N_x \times N_y \times N_z$	$600 \times 400 \times 400$

Regarding molecular transport, the diffusion driven by pressure gradients, the Soret effect associated with thermal diffusion, and the Hirschfelder and Curtiss approximation [48] are adopted. Every time iteration, the coefficients of the binary diffusion, and of the n-th species thermo-diffusion are evaluated, exploiting the expression from kinetic theory, while the viscosity and the thermal conductivity are estimated a priori using software libraries [49,50]. The average properties of the mixture are computed as follows: the viscosity is estimated by exploiting Wilke's expression along with the correction implemented by Bird [51,52], while the thermal conductivity is calculated with Mathur's expression [51,53]. Finally, the Hirschfelder and Curtiss law [48] is used to model preferential diffusion terms.

The chemical kinetics mechanism employed in this study is that of Gotama [54], which is tailored for NH_3/H_2-air combustion. The mechanism includes 24 different species and 119 elementary reactions.

The simulations are performed with HeaRT [55–58], an in-house developed parallel code, in conjunction with ENEA's supercomputing facility CRESCO [59]. The HeaRT code solves the compressible N-S equations alongside the species transport equations, which are discretized with finite-difference staggered schemes. The N-S equations are filtered to perform LES simulations, and closure terms are modeled through the Smagorinsky's subgrid scale model [60]. The diffusive fluxes are determined with a second-order centered scheme, while convective terms are handled using the $AUSM^{+}$-up method [61], coupled with a third/fifth-order $WENO$ to minimize spurious oscillations. Extended non-reflecting boundary conditions [62–64] are implemented at open boundaries to account for the effect of variable transport properties [65] and local heat release [66]. A synthetic generator of turbulence is employed at the air crossflow inlet [67].

4. Results

4.1. Instantaneous Flow Features

The flow fields and their characteristics are presented and discussed in this section. In Figure 4, the NH_3 mass fraction iso-surface colored by temperature is depicted as volume rendering for two simulations' set cases of Table 2 (i.e., Set #1 and Set #3). In the same renderings, a slice with the vorticity magnitude referring to the central longitudinal plane is depicted.

As the jet penetrates the transversal air stream, especially for high-momentum flux ratios, J, it mimics an obstacle like a cylinder invested by a flow. The crossflow bends the jet and a horse-shoe vortex is produced in front of the windward side exit of the jet; ring-like vortices emerge from the jet exit; a shear layer grows in the windward side, exhibiting a

Kelvin–Helmholtz hydrodynamic instability with its vortex dynamics (roll-up and pairing) up to the formation of small dissipative structures; and another shear layer, typically characterized by smaller eddies, grows in the leeward side of the jet. On the leeward side of the jet, a large recirculation zone, characterized by longer residence times, takes place. Such a complex fluid dynamic structure plays an important role in mixing, flame anchoring, combustion dynamics, and pollutant emission.

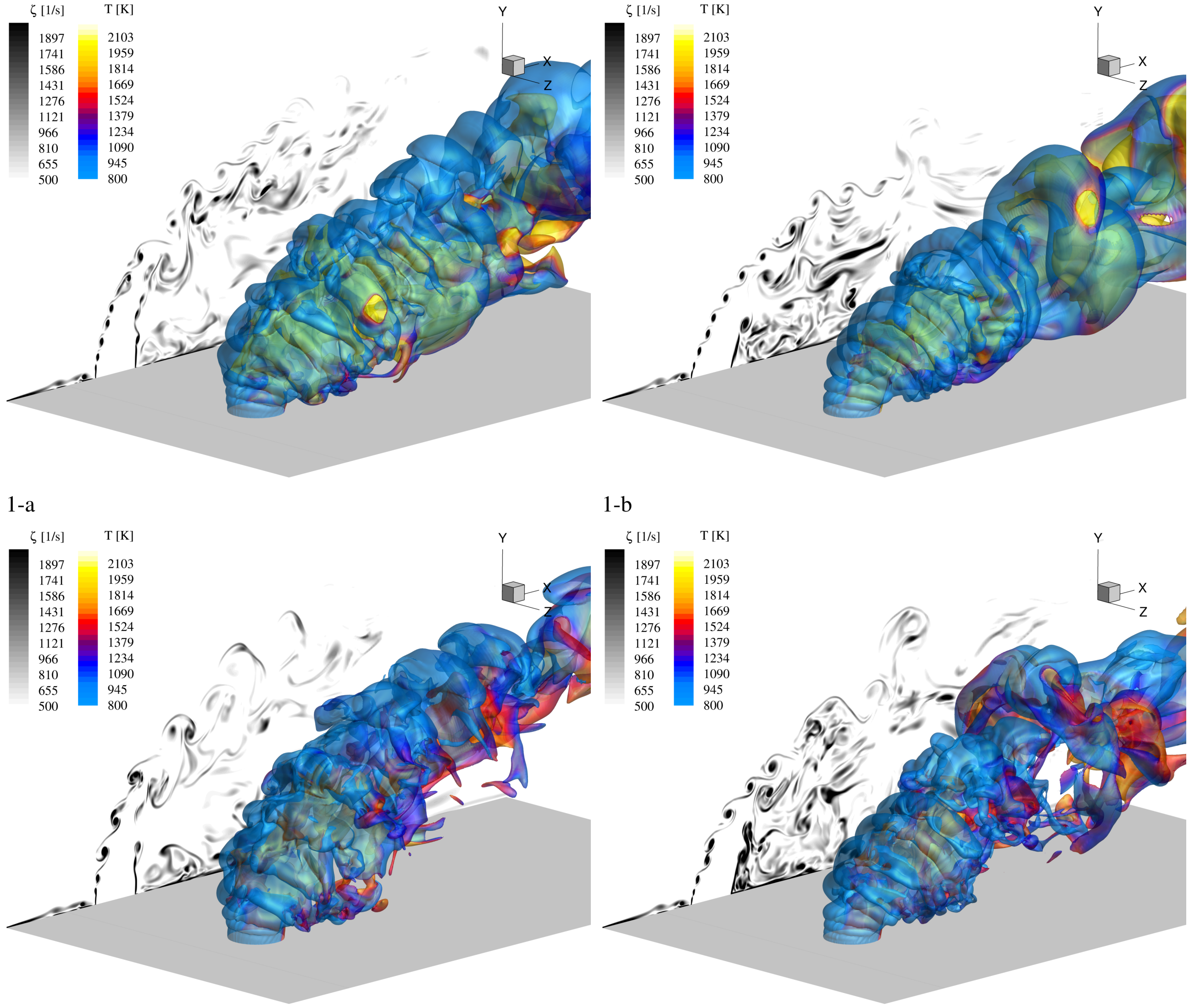

1-a

1-b

3-a

3-b

Figure 4. Instantaneous volume rendering of $Y_{NH_3} = 0.152$ mass fraction colored by the local value of the temperature (magma color map). On the backplane, it is represented the vorticity magnitude of the plane at z = 0 (greyscale color map). The rendering refers to t = 0.00647 s from the beginning of the computation. Each figure has indication of the specific case, e.g., 1-a refers to set #1 with 90° injection angle.

As expected, the present cases show that the fuel jet plume exhibits a lower penetration when the injection angle is 75°. Keeping constant the injection angle, the penetration is lower at 15% H_2 content in the fuel mixture, due to the lower momentum flux ratio. Differences can be observed in the Kelvin–Helmholtz hydrodynamic instabilities on the windward shear layer for different fuel mixture compositions. Particularly, when the H_2 content increases, the scale of the vortexes that develop in the shear layer increases as well. Another difference is the shedding frequency, which tends to increase as the H_2 content decreases. This phenomenon is also present, albeit to a lesser extent, on the leeward flame side, but it is not clearly visible. These conclusions are valid for both injection angles. The major effect of the injection angle on the windward shear layer is on the distance from the injection hole of the roller disruption. Indeed, when α varies from 90° to 75°, the shear layer breakup is retarded.

4.2. Averaged Combustion Characteristics

The fuel jet penetration is firstly investigated. From the averaged fields, the jet trajectory is estimated based on the y-component velocity (U_y). The jet trajectory provides a quantitative measure of how far the jet penetrates into the crossflow before being deflected, which is directly influenced by the jet's momentum. The equation used to estimate the jet trajectory is the common correlation developed by Pratte and Baines [68], which is

$$\frac{y}{\sqrt{J}d} = A\left(\frac{x}{\sqrt{J}d}\right)^{B}, \tag{2}$$

where x and y are the spatial coordinates of the trajectory, J is the momentum flux ratio, d is the jet diameter, and A and B are two constants that account for other relevant physical properties. Numerically, the trajectory is calculated by fitting Equation (2) along the flow field to find the A and B constants, ensuring that the calculated path follows the actual behavior observed in the simulation. The results of Figure 5 present the y-component mean velocity field for all cases, where each contour plot is accompanied by a white solid line representing the estimated jet trajectory. The matching obtained is quite satisfactory in all cases, although Equation (2) was originally designed for non-reacting jets. Indeed, the jet trajectory in non-reacting JICF experiments has been extensively studied and well characterized, while few correlations for reacting jets have been proposed [25,69–72]. Nevertheless, in some cases, correlations developed for a non-reacting JICF have been successfully applied to predict the trajectory in reacting situations [25,69], while other studies have observed significant deviations [70,71]. In the present cases, the trajectory fitting procedure yells for a fixed value of $B = 0.38$ and a variable value of A with the H_2 composition. The fitting results are shown in the largest subplot of Figure 5, which provides a quantitative assessment of the trajectory parameter A. As the hydrogen content increases, parameter A exhibits an ascending trend, reflecting the modification in jet penetration and deflection characteristics due to varying composition.

Figure 6 depicts the time-averaged mixture fraction contours on the $z = 0$ and $y = 0.003$ m planes; it also reports the stream traces, represented with white solid lines, and the stoichiometric mixture fraction, represented with a solid purple line. The stream traces emphasize the existence of a major recirculation zone that arises on the leeward side for all cases under investigation. This vortical structure has a peculiar shape in the space; indeed, most of the structure is initially aligned with the crosswise direction but, as the flow develops, it curves simultaneously in the streamwise and wall-normal directions, strongly deviating and mixing the incoming fresh air. This shape changes across the cases and seems to be stronger at $\alpha = 90°$. Cases 1-a and 4-a show also the presence of a second recirculation bubble above the previous one.

The pattern of the mixture fraction, and its stoichiometric value, in the field give information about the mixing in the zone under inspection. In case 1-a, almost the entire leeward branch has a mixture fraction greater than the stoichiometric value, and the presence of the second recirculation zone further promotes this effect. This is the case that achieves the best mixing and, as observed later, the best combustion performance in terms of temperatures (see Figure 7). In case 1-b, on the other hand, the second recirculation zone is not present but good mixing is obtained overall. By keeping the injection angle constant and increasing the hydrogen content, the situation changes dramatically. At 30% H_2, the mixing is greatly reduced (case 2-a) and is strongly driven by the recirculation zones. Moving to 45% (3-a) and then to 60% (4-a), the situation turns out to be similar, with a further decrease of the rich zones in the crosswise direction but an increase in the streamwise one. The same conclusions can be replicated for the 75° cases. In these cases, however, in the z = 0 plane, the recirculation zone turns out to be absent in the crosswise direction, strongly limiting the formation of rich zones only at the shear layer of the jet.

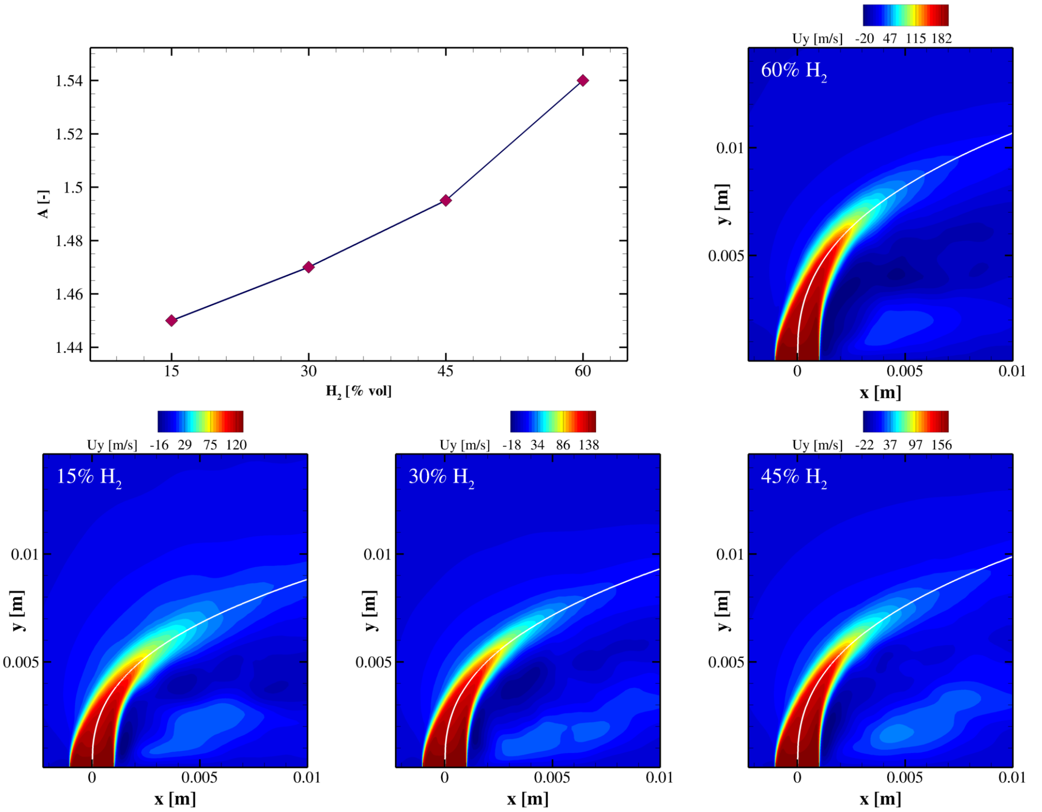

Figure 5. Time -averaged y-component velocity contours and variation of the A parameter of Equation (2) with the H_2 composition (top left). The white solid lines in each contour plot represent the numerically estimated jet trajectory based on Equation (2).

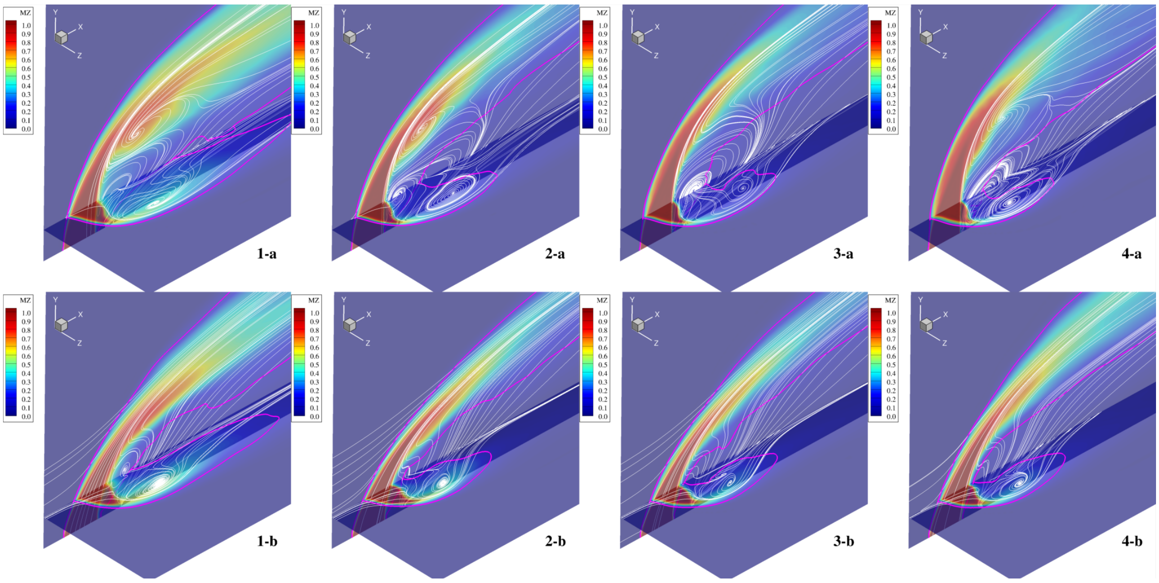

Figure 6. Time-averaged mixture fraction contours in the z = 0 and y = 0.003 m planes. The white solid lines represent the stream traces tangent to each plane, while the solid purple line indicates the mixture fraction stoichiometric value. Each figure has indication of the specific case, e.g., 1-a refers to set #1 with 90° injection angle.

Figure 7 reports the averaged temperature contour maps on the symmetry plane z = 0. As in our previous study [10], the windward flame is absent, while on the leeward side it is anchored in the shear layer near the jet exit, which is consistent with Grout et al. [73]. In this branch, a broad reaction zone arises, which is driven by the presence of a recirculation bubble (allowing longer residence times), and in almost all cases the maximum temperature reaches 2600 K.

The figure also highlights that the most intense combustion occurs at 15% H_2 and $\alpha = 90^\circ$ (1-a), with a maximum temperature that exceeds 2800 K. At a fixed injection angle, increasing the hydrogen content first leads to a reduction in the combustion intensity (2-a), which, however, increases again for higher values of H_2 (3-a and 4-a). A similar trend occurs for $\alpha = 75^\circ$, even if the lower injection angle decreases the combustion intensity and the extension of the combustion zone in the wall-parallel direction, giving rise to a spotted concave cold area near the wall. We can readily notice the attempted quenching of case 2-b due to the combination of low injection angle and low hydrogen concentration. Case 1-b exhibits a temperature peak around 2800 K, as for case 1-a, but in this case this zone is confined in the recirculation bubble. The peculiar behavior at 15% H_2 can be explained by a more intense hydrogen conversion through ammonia cracking and other formation pathways, which are analyzed in detail in Section 4.3.

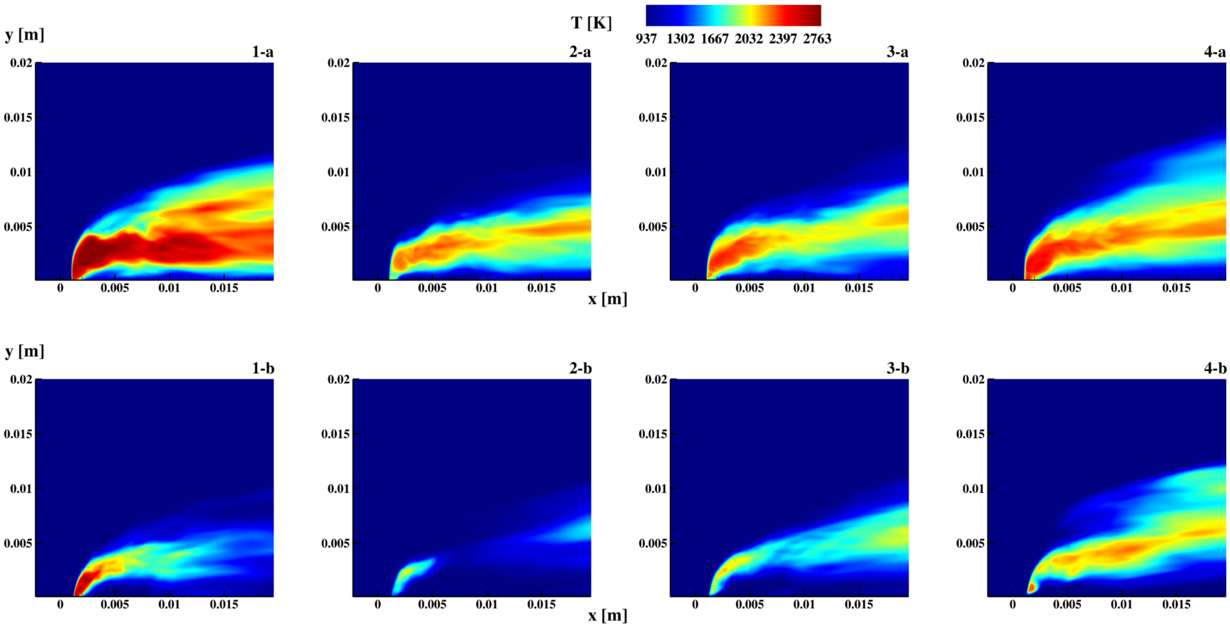

Figure 7. Time-averaged temperature contours on the central longitudinal x–y plane. Each figure has indication of the specific case, e.g., 1-a refers to set #1 with 90° injection angle.

Figure 8 shows the averaged NO mass fraction contour maps on the same x–y plane. At $\alpha = 90^\circ$, NO formation primarily occurs just downstream of the fuel injection point, reaching a maximum value that exceeds 16,000 dppm, and closely following the temperature distribution, though confined to a slightly narrower region (see Figure 7). For this reason, it is clear that the NO formation is not solely driven by the thermal pathway [74], as also shown in Section 2. When α varies to 75°, the spreading of the NO formation is reduced, following again the high-temperature regions. Nevertheless, the levels reached at this injection angle are of the same level of magnitude as the previous one, suggesting the presence of other mechanisms controlling this phenomenon.

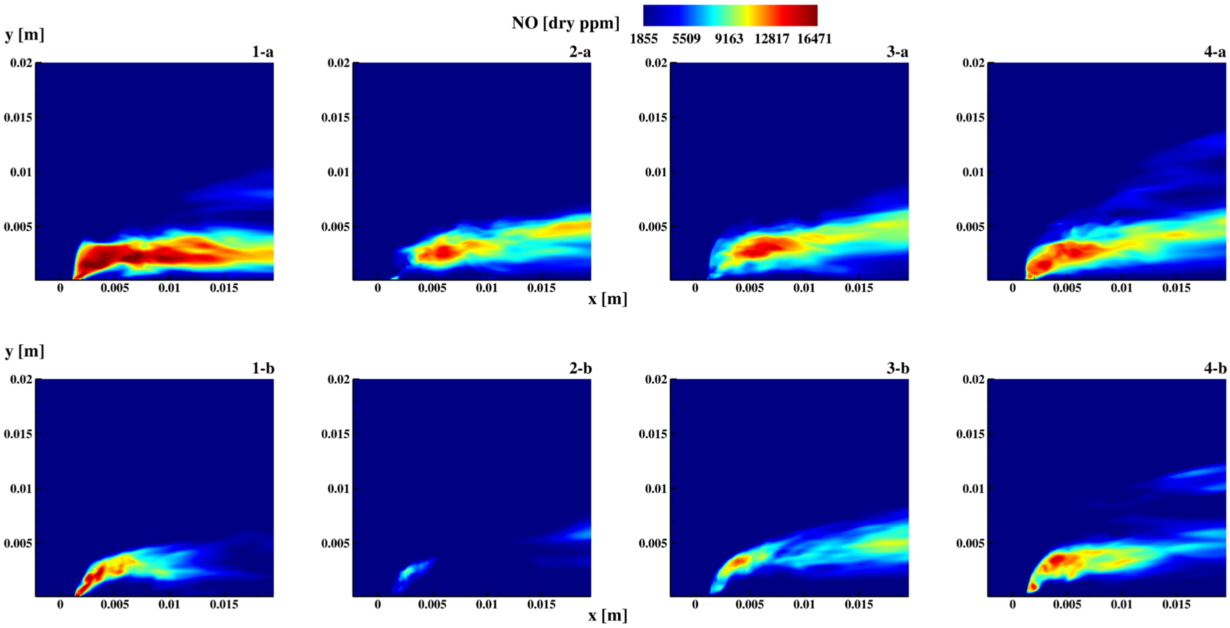

Figure 8. Time-averaged NO mass fraction concentrations contours on the central longitudinal x–y plane. Each figure has indication of the specific case, e.g., 1-a refers to set #1 with 90° injection angle.

4.3. Characteristic Formation Pathways of NO and H_2

This section provides some insights on the formation pathways of NO and H_2 in the investigated flames. In the present statistical analysis, the mixture fraction, Z, will play an important role. In the following, the Favre filtered mixture fraction, $\tilde{Z}$, is calculated following the definition of Z in the study of Tang et al. [75] on a non-premixed $NH_3/H_2/N_2$ jet flame:

$$Z = \frac{(Y_H - Y_{H,2})/2W_H - (Y_O - Y_{O,2})/W_O}{(Y_{H,1} - Y_{H,2})/2W_H - (Y_{O,1} - Y_{O,2})/W_O}. \tag{3}$$

Here, $Y_{O(H)}$ and $W_{O(H)}$ are the O(H) species local elemental mass fractions and atomic masses, respectively. The 1 and 2 subscripts refer to the fuel jet and the air crossflow, respectively. Statistics were collected for a time of 0.003 s, corresponding approximately to the time required for an air particle to travel across the computational domain (this approximation underestimates the convective time since it does not include the effect of combustion on flow velocity).

Figure 9a shows the normalized Probability Density Function (PDF) of the Favre filtered mixture fraction, $\tilde{Z}$, in the investigated flames. These PDFs show two peaks at Z = 0 and Z = 1, corresponding to air and fuel streams, and a further peak for Z values below 0.2, with tails extending to Z = 0.7. The a-flames have this third peak exactly on the stoichiometric value Z = 0.1403 (the same for all concentrations), apart from those at 15% H_2 (Z = 0.13); instead, the b-flames, apart from those at 30% that exhibit localized extinctions, have this peak at Z = 0.085, with the value decreasing as the hydrogen increases. Flames at 15% and 60% H_2 show the presence of rich zones at $Z > 0.3$, with this phenomenon being more pronounced for the 1-a flame. This result is in agreement with the joint-PDFs in Figure 10, where NO is formed also in rich zones of the flame but only for the flames 1a-b and 4a-b (even if in small concentrations). Figure 9b shows the same Probability Density Function colored by the mean temperature: in the simulated flames, the average temperature reaches its maximum for Z values between 0.08 and 0.2, apart from the flames with 15% hydrogen (and to a lesser extent for those with 60%), for which the maximum temperature region extends up to Z = 0.4 (Z = 0.25 for those with b), well beyond the stoichiometric mixture fraction value.

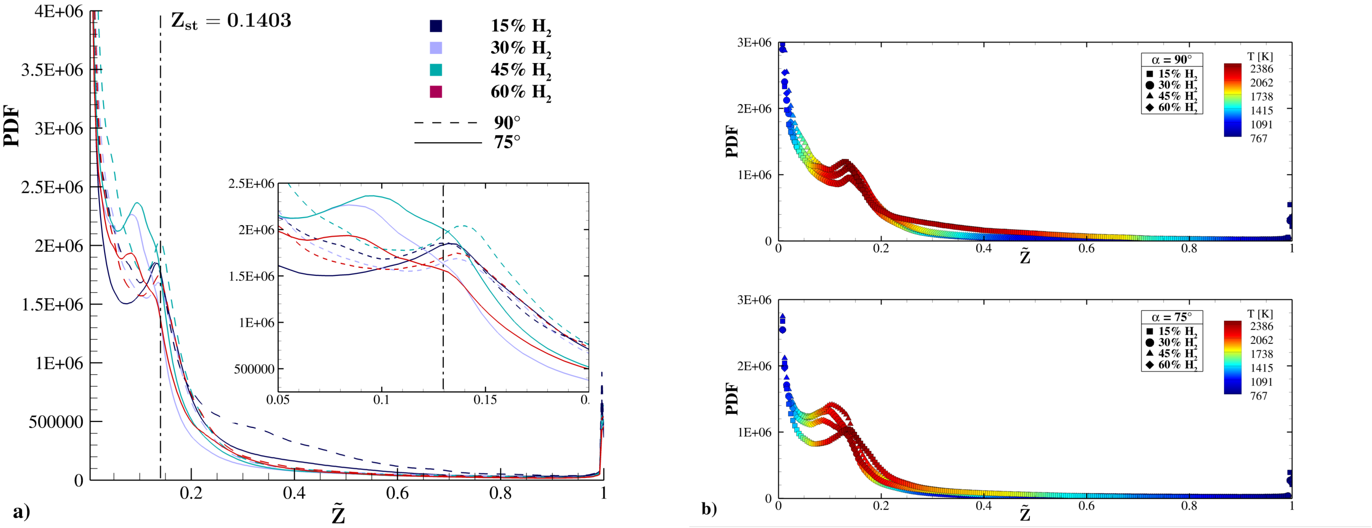

Figure 9. (**a**) Probability Density Function (PDF) of the Favre filtered mixture fraction, $\tilde{Z}$; (**b**) PDF of the Favre filtered mixture fraction, $\tilde{Z}$, colored with temperature.

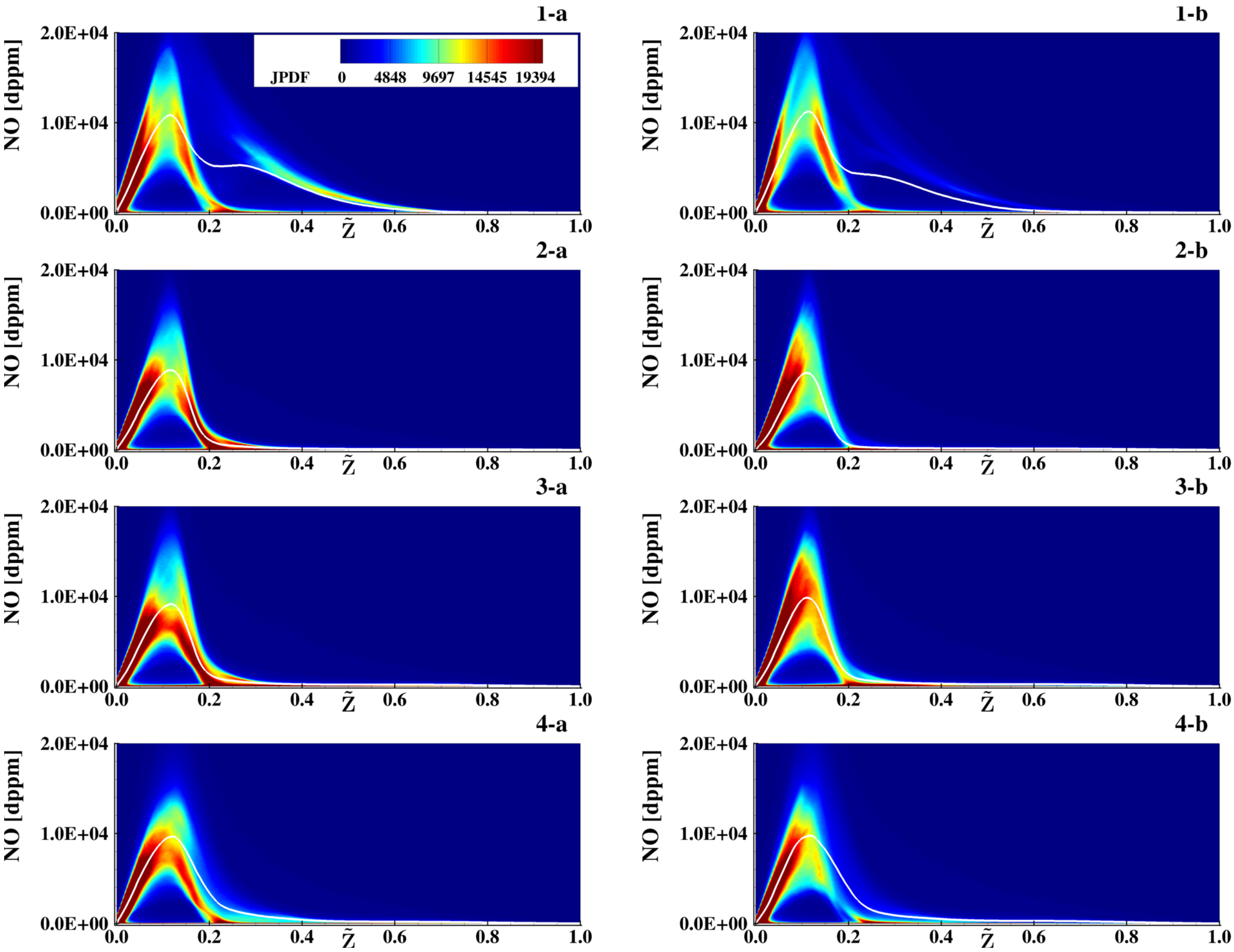

Figure 10. Joint-PDF of the NO concentration (dry-ppm) and mean NO concentration (solid line) versus the Favre filtered mixture fraction, $\tilde{Z}$. White solid line: mean NO concentration as a function of mixture fraction, $\tilde{Z}$. Each figure has indication of the specific case, e.g., 1-a refers to set #1 with 90° injection angle.

Figure 10 shows the joint-PDF of the NO dry-ppm (dppm) concentration. The maximum peak of NO concentration is reached in the flames with the highest ammonia content near the stoichiometric region (approximately around Z = 0.11 for all the fuel mixtures). All flames have a high probability of finding NO concentrations lower than 5000 dppm for $\tilde{Z}$ values lower than 0.05 (lean part of the flame), while those with an injection angle of 90 degrees also have a probability of finding NO concentrations lower than 200 dppm for $\tilde{Z}$ values higher than 0.2 (rich part of the flame). As can be seen from the comparison between the joint-pdf and the mean value (solid line), the latter tends to better fit the joint-pdf distribution (in the stoichiometric region) as the hydrogen content in the fuel increases, resulting in a lower probability of finding local flame extinctions. This deviation is more evident for flames with an angle of 75 degrees fuel injection. It is also interesting to note that the flames at 15% and 60% H_2 are the only ones that show high NO concentrations for mixture fraction values greater than 0.2, corresponding to very rich combustion conditions.

Figure 11 shows mean N_2O, NO_2 concentrations for the complete set of simulations as a function of the mixture fraction. In general, NO_2 concentrations are an order of magnitude smaller than N_2O and are produced mostly for lean values of the mixture fraction. N_2O at a low temperature is produced by the reaction R36 ($NH_2 + NO_2 = H_2O + N_2O$) and at all temperatures by R58 ($NH + NO = N_2O + H$) at the expanse of NO (flame 3a-b has the lowest average NO value in the rich zones, compared with the other stable flames, see Figure 10). It is predominantly consumed by the reaction R105 ($N_2O + H = N_2 + OH$). At all temperatures, NO_2 is produced at the expense of NO by the reaction R104 ($NO + HO_2 = NO_2 + OH$), while it is consumed by its reaction with H, NH_2 through the reactions R107 ($NO_2 + H = NO + OH$), R37 ($NH_2 + NO_2 = H_2NO + NO$), and R36 ($NH_2 + NO_2 = N_2O + H_2O$).

Figure 12 shows the mean scalar dissipation rate $\varnothing = 2D|\nabla Z|^2$, calculated at the plane $z = 0\,\mathrm{m}$, with $D = \lambda\rho/c_p$, λ being the thermal conductivity, ρ the density, and c_p the specific heat of the mixture, respectively. This quantity is similar to the inverse of a residence time, and affects both temperature and NO production. As the hydrogen increases, the high scalar dissipation rate region extends for increasingly larger values of coordinate y. The scalar dissipation rate reaches its peak values around the fuel jet core, with slightly higher values in the leeward part of the jet (~3000–5000 s^{-1}). In the a-flames, a zone of high scalar dissipation rate (~500 s^{-1}) is present in the recirculation region inclined at an angle of about ~16 degrees: this region tends to vanish as the hydrogen concentration in the fuel increases.

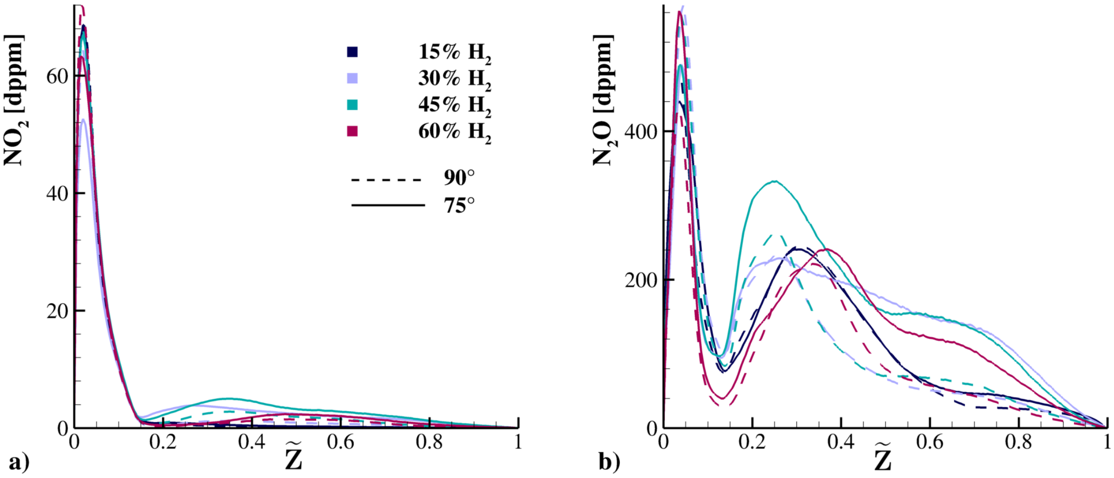

Figure 11. (**a**) Mean NO_2 concentration (dppm) as a function of the Favre filtered mixture fraction, $\tilde{Z}$; (**b**) Mean N_2O concentration (dppm) as a function of the Favre filtered mixture fraction, $\tilde{Z}$, for the complete set of simulations.

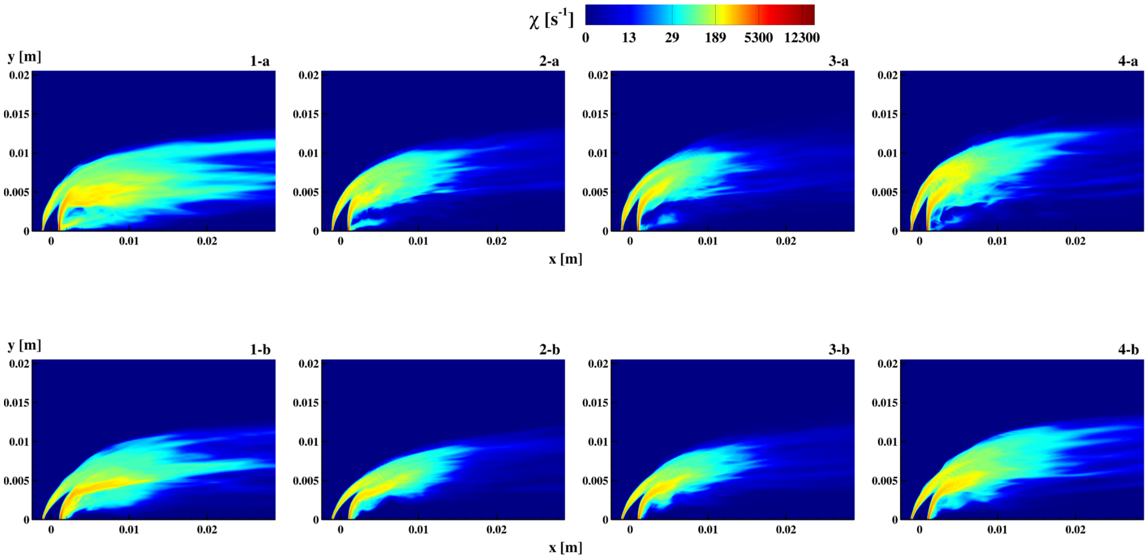

Figure 12. Mean scalar dissipation rate, χ, at the plane $z = 0$ m. Each figure has indication of the specific case, e.g., 1-a refers to set #1 with 90° injection angle.

As opposed to hydrocarbon flames, where the thermal pathway plays the most significant role, in ammonia/hydrogen flames, once NH_3 reacts with H, OH, O, forming NH_2 and NH, the NO formation is mainly due to the fuel pathways. The six more relevant NO formation pathways and their corresponding reactions are described in Table 3 [76], and their contribution to the NO mean rate of production versus the mixture fraction is shown in Figure 13. In every case, the HNO path is the most important one, followed by the NH_2 path, except for the 15% H_2 flames where the Zeldovich mechanism is the second in importance. Furthermore, while for the 15% H_2 flame the NO rate of production contributions have their peak at the same mixture fraction, i.e., close to the stoichiometric value and at ∼0.38 (that is, an order of magnitude larger), in the other cases the NO production pathways have their own peak at different locations, i.e., at mixture fraction values close to 0.2 and the stoichiometric value. The peaks reveal a monotonous trend, increasing with the increase in the hydrogen concentration. It should be noted that in the simulated time, identical for all flames, the 30% hydrogen flames exhibit localized extinctions (also highlighted in the average temperature profile in Figure 7); such extinctions do not occur in the other flames, even in the one with the lowest hydrogen concentration in the fuel jet (15%H_2), which furthermore exhibit the most extensive high-temperature region within the computational domain and the highest peaks.

Table 3. Synthesis of the reactions involved in the NO formation pathways. The dashed box highlights the reactions of the $DeNO_x$ process.

Reaction #	Chemical Expression	NO Pathway
R38	$NH_2 + NO = N_2 + H_2O$	N_2
R39	$NH_2 + NO = NNH + OH$	N_2
R59	$NH + NO = N_2 + OH$	N_2
R58	$NH + NO = N_2O + H$	N_2O
R102	$NH + O = NO + H$	NH_2
R101	$N + OH = NO + H$	Zeldovich
R64	$N + O_2 = NO + O$	Zeldovich
R63	$N_2 + O = N + NO$	Zeldovich
R97	$HNO + H = NO + H_2$	HNO
R103	$H + NO(+M) = HNO(+M)$	HNO
R98	$HNO + OH = NO + H_2O$	HNO
R107	$NO_2 + H = NO + OH$	NO_2
R108	$NO_2 + O = NO + O_2$	NO_2
R100	$NO_2(+M) = NO + O(+M)$	NO_2

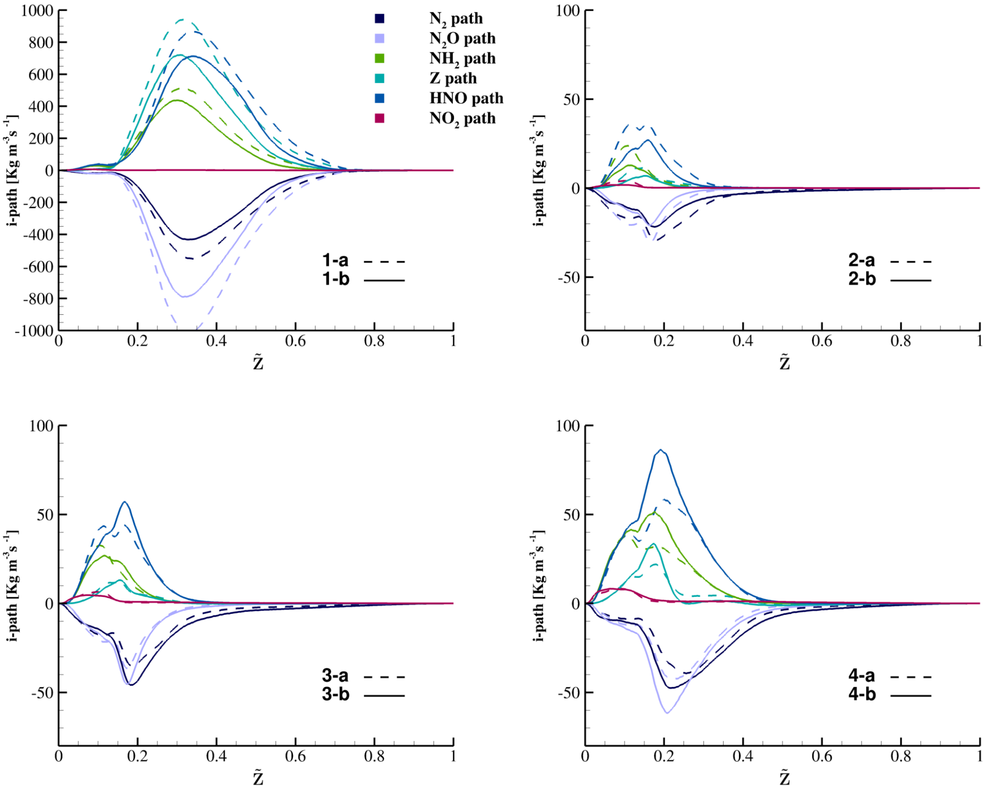

Figure 13. Mean rate of production (ROP) of the six NO formation pathways (see Table 3) as a function of the mixture fraction. Each figure has indication of the specific case, e.g., 1-a refers to set #1 with 90° injection angle.

Figure 14 shows the H_2 mean mass fraction at the plane z = 0 m for the complete set of flames. Flames 1a-b, which have the lowest concentration of H_2 in the fuel jet, show a peak value of H_2 within the reaction zone, similar to the maximum value of flames 3a-b, thus showing that in certain areas of the flame there is a strong production of H_2 deriving from the conversion of ammonia and its derivatives (NH, NH_2, N_2H_2, NNH). The H_2 production zones are localized immediately downstream of the fuel injection for $y > 0.004$ m (more pronounced for flame a), where the H_2 mass fraction peak is 0.068, which is very similar to the local hydrogen found in flames 3a-b. This peculiar effect of in situ cracking of NH_3 has recently been observed also by Alfazazi et al. [77,78], who have studied the characteristics of non-premixed flames in an axisymmetric bluff-body burner, giving the base for a strategy of direct, on-site combustion of NH_3 fuel.

Looking at the set of reactions involving H_2 production/destruction, as shown in Figure 15, in cases 1a-b the hydrogen is mainly consumed in regions with $Z < 0.3$ (through reactions involving the radicals H, O, OH, H_2O_2 denominated path-a) and produced at rich conditions with $Z \in [0.3–0.7]$, mainly through the reactions involving NH_3, NH, NH_2 (path-b), and secondarily by those involving NNH and N_2H_2 (path-c). It is stressed that this conversion phenomenon does not depend on the particular chemical mechanism here adopted, as the reactions causing it are present in all the other mechanisms typically used in the literature for ammonia and hydrogen flames with very similar reaction coefficients [43].

The most important reactions of path b are R50 $(NH + H = N + H_2)$, R52 $(2NH_2 = H_2NN + H_2)$, R31 $(H + NH_2 = NH + H_2)$, and R49 $(2NH_2 = N_2H_2 + H_2)$, while the direct conversion of NH_3 into H_2 R23 $(NH_3 + H = NH_2 + H_2)$ is the weakest. The transformation of NH_3 and its derivatives into H_2 increases its concentration in certain areas of the flame by three times the initial value in the fuel. The H_2 molecule compared with the ammonia molecule can therefore diffuse better within the reaction zone at high temperatures, contributing to a more stable flame with respect to flames 2a-b, which instead are more prone to exhibit localized extinctions.

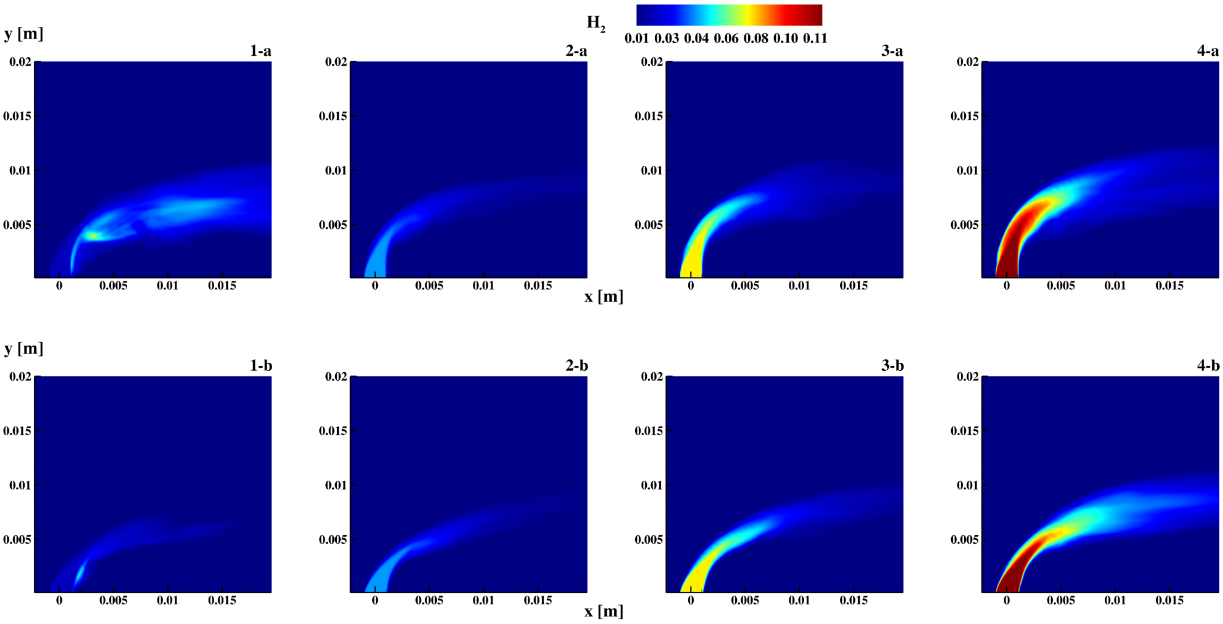

Figure 14. Mean H_2 mass fraction at the plane z = 0 m. Each figure has indication of the specific case, e.g., 1-a refers to set #1 with 90° injection angle.

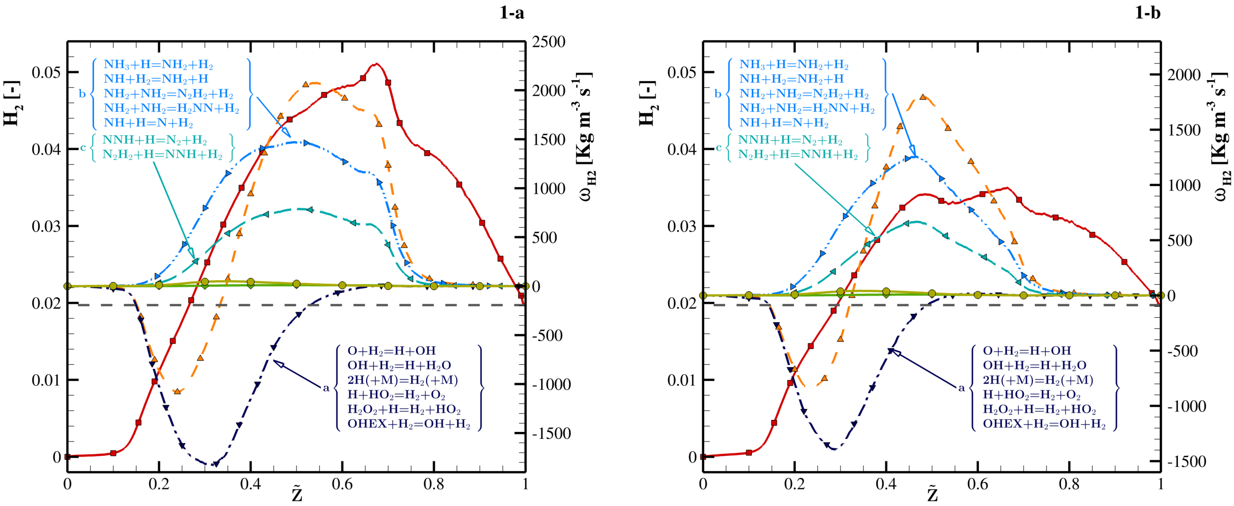

Figure 15. Hydrogen formation analysis versus the Favre filtered mixture fraction, $\tilde{Z}$, in flame 1a-b: H_2 mean mass fraction (—— ■); ω_{H_2} total formation rate (- - - ▲); i-th path ω_{H_2} formation rates (-··-·· ▶, -·-·- ▼, — — ◀, —— ●, —— ◆). The horizontal black dashed line represents the hydrogen mass fraction at the fuel jet inlet.

Figure 16 compares flames 1a-b and 4a-b close to the fuel injection, showing the mean NO concentration ([dppm]) and mixture fraction isolines at z = 0 m, isosurfaces of the scalar dissipation rate χ = 1250 s^{-1}, and velocity streamtraces in two different plane (x = 0.007 m and $x = 0.014$ m) to highlight how fresh air is transported in the recirculation zone in the two cases 4a-b. It is observed that the NO is mainly produced in two zones. The first is immediately adjacent to the fuel jet and exhibits high values of the scalar dissipation rate (increasingly higher values as the H_2 concentration in the fuel increases) and high values of the mixture fraction. This zone has a greater extent in the mixture fraction space for type b flames. The second zone is located in the recirculation zone downstream of the jet, and it exhibits low scalar dissipation rates ($\chi < 100\ \ \mathrm{s}^{-1}$) and Z values closer to the stoichiometric one, resulting in a very-high-temperature region. In general, for all flames, NO is produced for higher χ values as the mixture fraction and H_2 concentration in the fuel increase. The same trend occurs for the different NO formation paths except for the Zeldovich path, which is negligible for $Z > 0.25$.

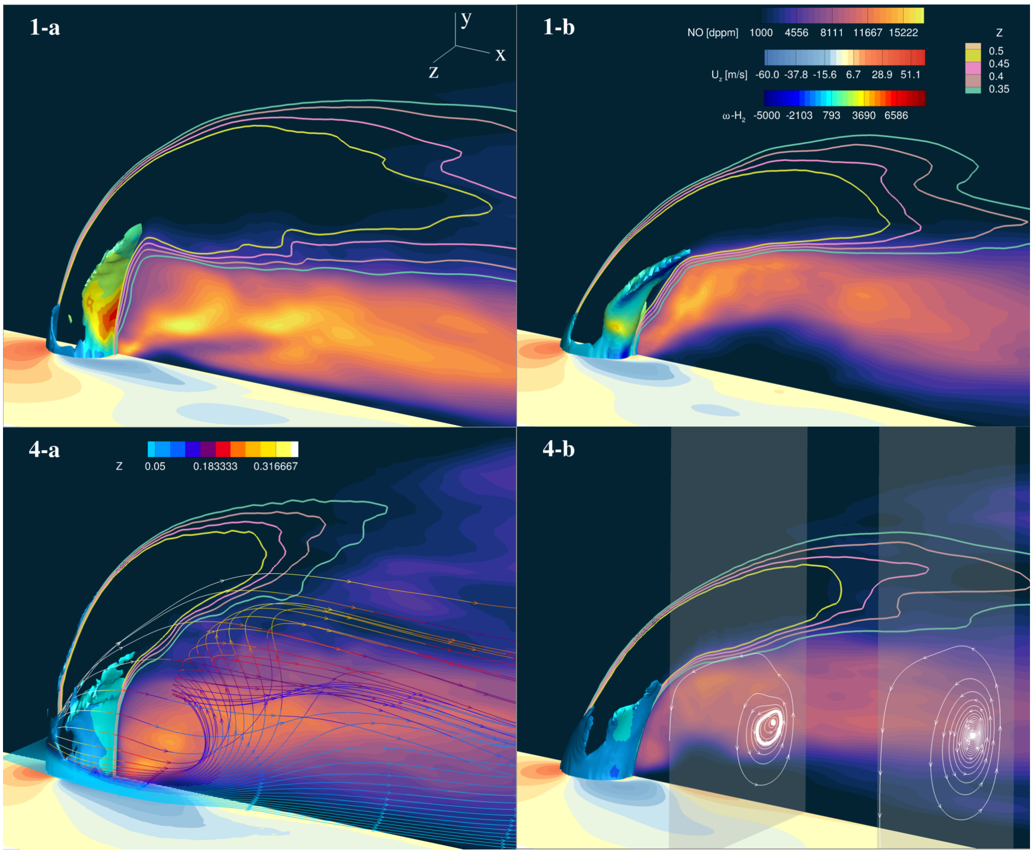

Figure 16. Mean NO [dppm] contour slice at $z = 0\,\mathrm{m}$. Colored lines are mean mixture fraction, $\tilde{Z}$, for the case 1a-b and 4a-b; scalar dissipation rate iso-surface at $\chi = 1250\ \ \mathrm{s}^{-1}$ colored by total $\omega_{H_2}\ \ [\mathrm{Kg\,m^{-3}s^{-1}}]$ production rate; mean $U_x\,[\mathrm{ms^{-1}}]$ velocity contour slice at $y = 0\,\mathrm{m}$; tridimensional streamtraces colored with mixture fraction in 4-a case; slice streamtraces at $x = 0.007\,\mathrm{m}$ and $x = 0.014\,\mathrm{m}$ in case 4-b. Each figure has indication of the specific case, e.g., 1-a refers to set #1 with 90° injection angle.

5. Conclusions

LES simulations of this set of eight flames show combustion trends that are not entirely expected.

- The flame with the lowest hydrogen content in the fuel jet has the highest temperatures, the highest NO production, and the lowest propensity to extinguish as it exhibits the highest conversion of ammonia to hydrogen. This phenomenon tends to decrease as the H_2 content increases in the fuel jet, and occurs in the leeward zone circumferentially and at the end of the fuel jet core. This subsequently allows the hydrogen to mix well with the air, which is transported by the vortices into the recirculation zone downstream of the jet, and to reach mixture fraction values close to the stoichiometric, thus leading to a large production of NO at higher temperature in comparison with the other flames. It is stressed that the ammonia-to-hydrogen conversion does not depend on the particular chemical mechanism here adopted, since the related reactions are also present in all the other mechanisms typically used in the literature for ammonia and hydrogen flames, with very similar reaction coefficients.

- The extent of the high-temperature recirculation zone (with a uniform mixture fraction close to stoichiometric) responsible for NO production is greater in a-type flames (90-degree angle); in b-type flames (75-degree angle), part of this region is occupied by a very lean mixture.
- At the exit of the combustion chamber, the flames with the highest hydrogen content (45–60% H_2) are those with the lowest NO concentration: among these, the b-flames are those that also present the lowest concentration of unburned fuel.

As a final remark related to the technology investigated in this work, present results demonstrate that the micro-mixing concept cannot be applied for non-premixed ammonia combustion, since NO pollutants are produced in large quantities in a region immediately after the fuel injection. A possible solution to be explored as a next step could be premixed combustion, with the adoption of a very lean $NH_3/H_2/N_2$-air mixture as fuel jet (the NO decreases for very lean and very rich flames).

Author Contributions: E.G., D.C., M.C.: original draft preparation and writing; D.C., M.C.: fluid dynamic simulation and statistical analysis; S.C., J.C.: laminar chemical kinetics simulations. All authors have read and agreed to the published version of the manuscript.

Funding: This study was performed within the Italian project "RICERCA E SVILUPPO DI TECNOLOGIE PER LA FILIERA DELL'IDROGENO POR-H2" ("Research and Development of Technologies for Hydrogen Chain", POR-H2, WP2, LA2.2.5), funded by the European Union (NextGeneraionEU) through the Italian Ministry of Environment and Energy Security, under the National Recovery and Resilience Plan (PNRR, Mission 2, Component 2, Investment 3.5, project code I83C22001170006).

Data Availability Statement: The original contributions presented in the study are included in the article, further inquiries can be directed to the corresponding author/s.

Acknowledgments: The computational resources and associated technical support utilised for this study were made available by the CRESCO/ENEAGRID High-Performance Computing infrastructure and its staff [59]. This computing infrastructure is funded by ENEA, the Italian National Agency for New Technologies, Energy, and Sustainable Economic Development, along with contributions from Italian and European research programmes (visit http://www.cresco.enea.it/english, accessed on 20 October 2023).

Conflicts of Interest: The authors declare no conflicts of interest.

References

1. Karim, H.; Natarajan, J.; Narra, V.; Cai, J.; Rao, S.; Kegley, J.; Citeno, J. Staged combustion system for improved emissions operability and flexibility for 7HA class heavy duty gas turbine engine. In Proceedings of the ASME Turbo Expo 2017: Turbomachinery Technical Conference and Exposition, Charlotte, NC, USA, 26–30 June 2017.
2. Pennell, D.A.; Bothien, M.R.; Ciani, A.; Granet, V.; Singla, G.; Thorpe, S.; Wickstroem, A.; Oumejjoud, K.; Yaquinto, M. An introduction to the ansaldo GT36 constant pressure sequential combustor. In Proceedings of the ASME Turbo Expo 2017: Turbomachinery Technical Conference and Exposition, Charlotte, NC, USA, 26–30 June 2017.
3. Goh, E.; Sirignano, M.; Li, J.; Nair, V.; Emerson, B.; Lieuwen, T.; Seitzman, J. Prediction of Minimum Achievable NOx Levels for Fuel-Staged Combustors. *Combust. Flame* **2019**, *200*, 276–285. [CrossRef]
4. Otero, M.; Genova, T., Jr.; Stiehl, B.; Morales, A.J.; Martin, S.; Ahmed, K.A. The Influence of Pressure on Flame-Flow Characteristics of a Reacting Jet in Crossflow. *ASME J. Energy Res. Technol.* **2021**, *144*, 052301. [CrossRef]
5. Stiehl, B.; Otero, M.; Genova, T.; Martin, S.; Ahmed, K. The Effect of Pressure on NOx Entitlement and Reaction Timescales in a Premixed Axial Jet-In-Crossflow. *ASME J. Energy Res. Technol.* **2021**, *143*, 112306. [CrossRef]
6. Lieuwen, T.; Chang, M.; Amato, A. Stationary Gas Turbine Combustion: Technology Needs and Policy Considerations. *Combust. Flame* **2021**, *160*, 1311–1314. [CrossRef]
7. Funke, H.W.; Beckmann, N.; Abanteriba, S. An overview on dry low NOx micromix combustor development for hydrogen-rich gas turbine applications. *Int. J. Hydrogen Energy* **2019**, *44*, 6978–6990. [CrossRef]
8. Noble, D.; Wu, D.; Emerson, B.; Sheppard, S.; Lieuwen, T.; Angello, L. Assessment of current capabilities and near-term availability of hydrogen-fired gas turbines considering a low-carbon future. *J. Eng. Gas Turbines Power* **2021**, *143*, 041002. [CrossRef]
9. Devriese, C.; Pennings, W.; de Reuver, H.; Penninx, G.; de Ruiter, G.; Bastiaans, R.; De Paepe, W. The Design and Optimisation of a Hydrogen Combustor for a 100 kW micro Gas Turbine. In *10th International Gas Turbine Conference, IGTC 2021: Gas Turbines in a Carbon-Neutral Society*; ETN: Brussels, Belgium, 2021; p. 19.

10. Giacomazzi, E.; Cecere, D.; Cimini, M.; Carpenella, S. Direct Numerical Simulation of a Reacting Turbulent Hydrogen/Ammonia/Nitrogen Jet in an Air Crossflow at 5 Bar. *Energies* **2023**, *16*, 7704. [CrossRef]
11. Yao, N.; Pan, W.; Zhang, J.; Wei, L. The advancement on carbon-free ammonia fuels for gas turbine: A review. *Energy Convers. Manag.* **2024**, *315*, 118745. [CrossRef]
12. Pfahl, U.; Ross, M.; Shepherd, J.; Pasamehmetoglu, K.; Unal, C. Flammability limits, ignition energy, and flame speeds in H2–CH4–NH3–N2O–O2–N2 mixtures. *Combust. Flame* **2000**, *123*, 140–158. [CrossRef]
13. Mathieu, O.; Petersen, E.L. Experimental and modeling study on the high-temperature oxidation of Ammonia and related NOx chemistry. *Combust. Flame* **2015**, *162*, 554–570. [CrossRef]
14. Normand, A. Method for Generating a Reducing Atmosphere for Heat-Treating Installations. US Patent 4,069,071, 17 January 1978.
15. Ganley, J.C.; Seebauer, E.G.; Masel, R.I. Development of a microreactor for the production of hydrogen from ammonia. *J. Power Sources* **2004**, *137*, 53–61. [CrossRef]
16. Sørensen, R.Z.; Nielsen, L.J.; Jensen, S.; Hansen, O.; Johannessen, T.; Quaade, U.; Christensen, C.H. Catalytic ammonia decomposition: Miniaturized production of COx-free hydrogen for fuel cells. *Catal. Commun.* **2005**, *6*, 229–232. [CrossRef]
17. Hayakawa, A.; Arakawa, Y.; Mimoto, R.; Somarathne, K.K.A.; Kudo, T.; Kobayashi, H. Experimental investigation of stabilization and emission characteristics of ammonia/air premixed flames in a swirl combustor. *Int. J. Hydrogen Energy* **2017**, *42*, 14010–14018. [CrossRef]
18. Hayakawa, A.; Ichikawa, A.; Arakawa, Y.; Kudo, T.; Kobayashi, H. Enhancement of Reaction and Stability of Ammonia Flames using Hydrogen Addition and Swirling Flows. In Proceedings of the 2015 NH3 Fuel Conference, Argonne National Laboratory, Chicago, IL, USA, 22 September 2015; Volume 22.
19. Khateeb, A.A.; Guiberti, T.F.; Zhu, X.; Younes, M.; Jamal, A.; Roberts, W.L. Stability limits and NO emissions of technically-premixed ammonia-hydrogen-nitrogen-air swirl flames. *Int. J. Hydrogen Energy* **2020**, *45*, 22008–22018. [CrossRef]
20. Khateeb, A.A.; Guiberti, T.F.; Wang, G.; Boyette, W.R.; Younes, M.; Jamal, A.; Roberts, W.L. Stability limits and NO emissions of premixed swirl ammonia-air flames enriched with hydrogen or methane at elevated pressures. *Int. J. Hydrogen Energy* **2021**, *46*, 11969–11981. [CrossRef]
21. Valera-Medina, A.; Marsh, R.; Runyon, J.; Pugh, D.; Beasley, P.; Hughes, T.; Bowen, P. Ammonia–methane combustion in tangential swirl burners for gas turbine power generation. *Appl. Energy* **2017**, *185*, 1362–1371. [CrossRef]
22. Nair, V.; Sirignano, M.D.; Schmidheiser, S.; Dillon, L.; Fugger, C.A.; Yi, T.; Jiang, N.; Hsu, P.S.; Slipchenko, M.N.; Roy, S.; et al. Tomographic PIV characterization of the near field topology of the reacting jet in crossflow. In Proceedings of the AIAA Scitech 2020 Forum, Orlando, FL, USA, 6–10 January 2020.
23. Zhang, X.; Wang, K.; Wen, X.; He, C.; Liu, Y.; Zhou, W. Experimental study of time-resolved simultaneous velocity and concentration fields of an inclined jet in crossflow. *Int. J. Heat Mass Transf.* **2022**, *188*, 122622. [CrossRef]
24. Tao, C.; Zhou, H. Effects of different preheated CO2/O2 jet in cross-flow on combustion instability and emissions in a lean-premixed combustor. *J. Energy Inst.* **2020**, *93*, 2334–2343. [CrossRef]
25. Roa, M.; Lamont, W.G.; Meyer, S.E.; Szedlacsek, P.; Lucht, R.P. Emission measurements and OH-PlIF of reacting hydrogen jets in vitiated crossflow for stationary gas turbines. In *Turbo Expo: Power for Land, Sea, and Air*; American Society of Mechanical Engineers: Houston, TX, USA, 2012; Volume 44687, pp. 491–498.
26. Ruiz, A.; Lacaze, G.; Oefelein, J. Flow topologies and turbulence scales in a jet-in-cross-flow. *Phys. Fluids* **2015**, *27*, 045101. [CrossRef]
27. Zhang, L.; Yang, V. Flow dynamics and mixing of a transverse jet in crossflow—Part I: Steady crossflow. *J. Eng. Gas Turbines Power* **2017**, *139*, 082601. [CrossRef]
28. Cheng, M.; Wang, H.; Luo, K.; Fan, J. A direct numerical simulation study on the structures and turbulence–flame interactions of a laboratory-scale lean premixed jet flame in cross-flow. *J. Fluid Mech.* **2023**, *957*, A27. [CrossRef]
29. New, T.; Lim, T.; Luo, S. Effects of jet velocity profiles on a round jet in cross-flow. *Exp. Fluids* **2006**, *40*, 859–875. [CrossRef]
30. Zhang, Z.; Abdelsamie, A.; Chi, C.; Thevenin, D.; Luo, K.H. Combustion mode and mixing characteristics of a reacting jet in crossflow. *Energy Fuels* **2021**, *35*, 13325–13337. [CrossRef]
31. Jain, N.; Seitzman, J.M. Mixing and combustion characterization of a staged combustor with multiple, high mass-ratio jets in crossflow. In *Turbo Expo: Power for Land, Sea, and Air*; American Society of Mechanical Engineers: Charlotte, NC, USA, 2017; Volume 50855, p. V04BT04A064.
32. You, C.H.; Lee, H.Y.; Hwang, S.S. Low NOX combustion characteristics by hydrogen micro jet flame in cross flow. *J. Mech. Sci. Technol.* **2023**, *37*, 445–455. [CrossRef]
33. Minamoto, Y.; Kolla, H.; Grout, R.W.; Gruber, A.; Chen, J.H. Effect of fuel composition and differential diffusion on flame stabilization in reacting syngas jets in turbulent cross-flow. *Combust. Flame* **2015**, *162*, 3569–3579. [CrossRef]
34. Kolla, H.; Grout, R.; Gruber, A.; Chen, J. Transverse fuel jet in turbulent cross-flow: Influence of fuel composition on near field flame stabilization. In Proceedings of the 8th US National Combustion Meeting, Park City, UT, USA, 19–22 May 2013.
35. Kolla, H.; Grout, R.W.; Gruber, A.; Chen, J.H. Mechanisms of flame stabilization and blowout in a reacting turbulent hydrogen jet in cross-flow. *Combust. Flame* **2012**, *159*, 2755–2766. [CrossRef]
36. Chan, W.L.; Kolla, H.; Ihme, M.; Chen, J.H. Analysis of a jet in cross flow using an unsteady flamelet model. In Proceedings of the Spring Technical Meeting of the Central States Section of the Combustion Institute, Dayton, OH, USA, 22–24 April 2012.

37. Chan, W.L.; Kolla, H.; Chen, J.H.; Ihme, M. Assessment of model assumptions and budget terms of the unsteady flamelet equations for a turbulent reacting jet-in-cross-flow. *Combust. Flame* **2014**, *161*, 2601–2613. [CrossRef]
38. Kroniger, D.; Horikawa, A.; Funke, H.H.W.; Pfaeffle, F.; Kishimoto, T.; Okada, K. Experimental and numerical investigation on the effect of pressure on micromix hydrogen combustion. In Proceedings of the Turbo Expo: Power for Land, Sea, and Air, ASME Turbo Expo 2021: Turbomachinery Technical Conference and Exposition, Virtual, Online, 7–11 June 2021; Volume 84942, p. V03AT04A025.
39. Yu, X.; Chen, T.; Zhang, Q.; Wang, T. CFD simulations of quenching process for partial oxidation of methane: Comparison of jet-in-cross-flow and impinging flow configurations. *Chin. J. Chem. Eng.* **2018**, *26*, 903–913. [CrossRef]
40. Cuoci, A.; Frassoldati, A.; Faravelli, T.; Ranzi, E. OpenSMOKE++: An object-oriented framework for the numerical modeling of reactive systems with detailed kinetic mechanisms. *Comput. Phys. Commun.* **2015**, *192*, 237–264. [CrossRef]
41. Cuoci, A.; Frassoldati, A.; Faravelli, T.; Ranzi, E. Numerical modeling of laminar flames with detailed kinetics based on the operator-splitting method. *Energy Fuels* **2013**, *27*, 7730–7753. [CrossRef]
42. Puri, I.; Seshadri, K. Extinction of diffusion flames burning diluted methane and diluted propane in diluted air. *Combust. Flame* **1986**, *65*, 137–150. [CrossRef]
43. Alnasif, A.; Mashruk, S.; Shi, H.; Alnajideen, M.; Wang, P.; Pugh, D.; Valera-Medina, A. Evolution of ammonia reaction mechanisms and modeling parameters: A review. *Appl. Energy Combust. Sci.* **2023**, *15*, 100175.
44. Cecere, D.; Giacomazzi, E.; Di Nardo, A.; Calchetti, G. Gas turbine combustion technologies for hydrogen blends. *Energies* **2023**, *16*, 6829. [CrossRef]
45. Xu, S.; Jin, S.; Tong, Y.; Shi, B.; Tu, Y.; Liu, H. Quantitative evaluation of NO formation and destruction routes during methane MILD combustion using an improved calculation method. *Fuel* **2022**, *324*, 124593. [CrossRef]
46. Chen, D.; Li, J.; Li, X.; Deng, L.; He, Z.; Huang, H.; Kobayashi, N. Study on combustion characteristics of hydrogen addition on ammonia flame at a porous burner. *Energy* **2023**, *263*, 125613. [CrossRef]
47. Medhat, M.; Yehia, M.; Franco, M.C.; Rocha, R.C. A numerical prediction of stabilized turbulent partially premixed flames using ammonia/hydrogen mixture. *J. Adv. Res. Fluid Mech. Therm. Sci.* **2021**, *87*, 113–133. [CrossRef]
48. Hirschfelder, J.O.; Curtiss, C.F.; Bird, R.B. *The Molecular Theory of Gases and Liquids*; John Wiley & Sons: Hoboken, NJ, USA, 1964.
49. Ern, A.; Giovangigli, V. *Multicomponent Transport Algorithms*; Springer Science & Business Media: Berlin/Heidelberg, Germany, 1994; Volume 24.
50. Ern, A.; Giovangigli, V. Fast and accurate multicomponent transport property evaluation. *J. Comput. Phys.* **1995**, *120*, 105–116. [CrossRef]
51. Bird, R.; Stewart, W.; Lightfoot, E. *Transport Phenomena*, 2nd ed.; John Wiley & Sons, Inc.: New York, NY, USA, 2006.
52. Wilke, C.R. A viscosity equation for gas mixtures. *J. Chem. Phys.* **1950**, *18*, 517–519. [CrossRef]
53. Mathur, S.; Tondon, P.; Saxena, S. Thermal conductivity of binary, ternary and quaternary mixtures of rare gases. *Mol. Phys.* **1967**, *12*, 569–579. [CrossRef]
54. Gotama, G.J.; Hayakawa, A.; Okafor, E.C.; Kanoshima, R.; Hayashi, M.; Kudo, T.; Kobayashi, H. Measurement of the laminar burning velocity and kinetics study of the importance of the hydrogen recovery mechanism of ammonia/hydrogen/air premixed flames. *Combust. Flame* **2022**, *236*, 111753. [CrossRef]
55. Giacomazzi, E.; Cecere, D. A combustion regime-based model for large eddy simulation. *Energies* **2021**, *14*, 4934. [CrossRef]
56. Giacomazzi, E.; Cecere, D.; Arcidiacono, N. Flame Anchoring of an $H_2/O_2/$ Non-Premixed Flamewith $O_2/$ Transcritical Injection. *Aerospace* **2022**, *9*, 707. [CrossRef]
57. Cecere, D.; Giacomazzi, E.; Arcidiacono, N. DNS of a non-premixed $CH_4//O_2/$ flame in a supercritical $CO_2/$ environment. *Fuel* **2024**, *362*, 130709. [CrossRef]
58. Cecere, D.; Giacomazzi, E.; Arcidiacono, N.; Picchia, F. Direct numerical simulation of a turbulent lean premixed $CH_4//H_2/$–Air slot flame. *Combust. Flame* **2016**, *165*, 384–401. [CrossRef]
59. Ponti, G.; Palombi, F.; Abate, D.; Ambrosino, F.; Aprea, G.; Bastianelli, T.; Beone, F.; Bertini, R.; Bracco, G.; Caporicci, M.; et al. The role of medium size facilities in the HPC ecosystem: The case of the new CRESCO4 cluster integrated in the ENEAGRID infrastructure. In Proceedings of the 2014 International Conference on High Performance Computing & Simulation (HPCS), Bologna, Italy, 21–25 July 2014; pp. 1030–1033.
60. Katopodes, N.D. *Free-Surface Flow: Environmental Fluid Mechanics*; Butterworth-Heinemann: Oxford, UK, 2018.
61. Liou, M.S. A sequel to AUSM, Part II: AUSM+-up for all speeds. *J. Comput. Phys.* **2006**, *214*, 137–170. [CrossRef]
62. Rudy, D.H.; Strikwerda, J.C. Boundary conditions for subsonic compressible Navier-Stokes calculations. *Comput. Fluids* **1981**, *9*, 327–338. [CrossRef]
63. Thompson, K.W. Time dependent boundary conditions for hyperbolic systems. *J. Comput. Phys.* **1987**, *68*, 1–24. [CrossRef]
64. Poinsot, T.J.; Lelef, S. Boundary conditions for direct simulations of compressible viscous flows. *J. Comput. Phys.* **1992**, *101*, 104–129. [CrossRef]
65. Baum, M.; Poinsot, T.; Thévenin, D. Accurate boundary conditions for multicomponent reactive flows. *J. Comput. Phys.* **1995**, *116*, 247–261. [CrossRef]
66. Sutherland, J.C.; Kennedy, C.A. Improved boundary conditions for viscous, reacting, compressible flows. *J. Comput. Phys.* **2003**, *191*, 502–524. [CrossRef]

67. Klein, M.; Sadiki, A.; Janicka, J. A digital filter based generation of inflow data for spatially developing direct numerical or large eddy simulations. *J. Comput. Phys.* **2003**, *186*, 652–665. [CrossRef]
68. Pratte, B.D.; Baines, W.D. Profiles of the Round Turbulent Jet in A Cross Flow. *J. Hydraul. Div.* **1967**, *93*, 53–64. [CrossRef]
69. Steinberg, A.; Sadanandan, R.; Dem, C.; Kutne, P.; Meier, W. Structure and stabilization of hydrogen jet flames in cross-flows. *Proc. Combust. Inst.* **2013**, *34*, 1499–1507. [CrossRef]
70. Hasselbrink, E.F.; Mungal, M. Transverse jets and jet flames. Part 2. Velocity and OH field imaging. *J. Fluid Mech.* **2001**, *443*, 27–68. [CrossRef]
71. Sullivan, R.; Wilde, B.; Noble, D.R.; Seitzman, J.M.; Lieuwen, T.C. Time-averaged characteristics of a reacting fuel jet in vitiated cross-flow. *Combust. Flame* **2014**, *161*, 1792–1803. [CrossRef]
72. Wagner, J.A.; Grib, S.W.; Renfro, M.W.; Cetegen, B.M. Flowfield measurements and flame stabilization of a premixed reacting jet in vitiated crossflow. *Combust. Flame* **2015**, *162*, 3711–3727. [CrossRef]
73. Grout, R.W.; Gruber, A.; Kolla, H.; Bremer, P.T.; Bennett, J.; Gyulassy, A.; Chen, J. A direct numerical simulation study of turbulence and flame structure in transverse jets analysed in jet-trajectory based coordinates. *J. Fluid Mech.* **2012**, *706*, 351–383. [CrossRef]
74. Somarathne, K.D.K.A.; Okafor, E.C.; Sugawara, D.; Hayakawa, A.; Kobayashi, H. Effects of OH concentration and temperature on NO emission characteristics of turbulent non-premixed CH4/NH3/air flames in a two-stage gas turbine like combustor at high pressure. *Proc. Combust. Inst.* **2021**, *38*, 5163–5170. [CrossRef]
75. Tang, H.; Yang, C.; Wang, G.; Krishna, Y.; Guiberti, T.F.; Roberts, W.L.; Magnotti, G. Scalar structure in turbulent non-premixed NH3/H2/N2 jet flames at elevated pressure using Raman spectroscopy. *Combust. Flame* **2022**, *244*, 112292. [CrossRef]
76. Shervin Karimkashi, P.; Tamadonfar, O.K.; Vuorinen, V. A Numerical Investigation on Effects of Hydrogen Enrichment and Turbulence on NO Formation Pathways in Premixed Ammonia/Air Flames. *Combust. Sci. Technol.* **2023**, 1–30. [CrossRef]
77. Alfazazi, A.; Es-sebbar, E.t.; Kumar, S.; Abdelwahid, S.; Asiri, A.H.; Zhao, W.; Im, H.G.; Dally, B. Effects of ammonia in-situ partial cracking on the structure of bluff-body non-premixed flames. *Proc. Combust. Inst.* **2024**, *40*, 105697. [CrossRef]
78. Alfazazi, A.; Elbaz, A.M.; Li, J.; Abdelwahid, S.; Im, H.G.; Dally, B. Characteristics of ammonia-hydrogen nonpremixed bluff-body-stabilized flames. *Combust. Flame* **2023**, *258*, 113066. [CrossRef]